4 Implementation and Numerical Examples

Programming is understanding.
— Kristen Nygaard —

The solution of the linear KKT-complementarity problems arising as subproblems in the inexact continuation algorithm developed in Chapter 3 is not the main topic of this thesis and will only be sketched here. Subsequently, numerical examples are given.

4.1 Solution of Linear Subproblems

In this section we will sketch the computation of the inexact Newton corrections δv^k and inexact tangential predictors p_k. Both reduce to the task of solving linear operator equations

$$Av = b \tag{4.1}$$

in Banach space up to a specified accuracy, where the operator $A : V \to Z$ consists of Nemyckii and differential operators. For the complementarity formulation of optimal control problems, it represents a differential algebraic equation boundary value problem.

Discretization

For the discretization of linear differential algebraic boundary value problems, several methods can be employed, such as multiple shooting or collocation. For a more detailed presentation we refer to the textbook by Ascher, Mattheij, and Russell [2]. The current implementation uses a finite element discretization in order to be able to experiment with different complementarity formulations involving direct representation of measure valued Lagrange multipliers. Note that for the suggested approach the finite element discretization is computationally equivalent to the collocation approximation.

The implemented finite element method is a Petrov-Galerkin discretization which uses ansatz functions with local support, spanning a finite dimensional subspace $V_h \subset V$. Using an appropriately chosen subspace $Z_h^* \subset Z^*$ with the same dimension, the operator equation (4.1) is required to hold for the

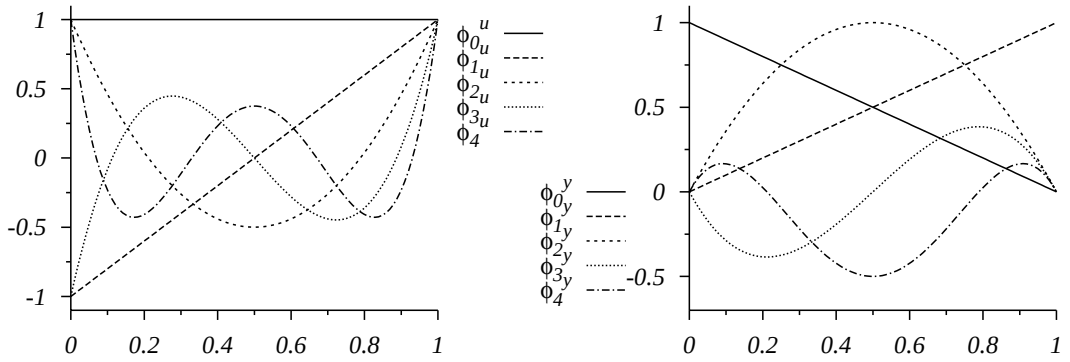

Figure 4.1: Finite element ansatz functions up to order four for the controls (left) and for the states (right). The state ansatz functions ϕ_0 and ϕ_1 are nodal hat functions that extend to the neighboring grid intervals.

approximate solution $v_h \in V_h$ in a weak sense:

$$\langle Av_h - b, \zeta \rangle = 0 \quad \text{for all } \zeta \in Z_h^* \tag{4.2}$$

With the finite element bases $\{\phi_i\} \subset V_h$, $\{\zeta_i\} \subset Z_h^*$, and the solution representation $v_h = \sum_i \alpha_i \phi_i$, the weak formulation (4.2) is equivalent to

$$A_h \alpha - \beta = 0$$

with $\beta_i = \langle b, \zeta_i \rangle$ and $(A_h)_{ij} = \langle A\phi_i, \zeta_j \rangle$.

The local support of the base functions ϕ_i and ζ_i in combination with Nemyckii and differential operators leads to a sparse discrete system, which can efficiently be represented as a banded system in the case of ordinary differential equations. Piecewise polynomials of arbitrary but fixed degree as depicted in Figure 4.1 have been used as ansatz functions on an adaptively refined grid.

Solving Discrete KKT-Complementarity Systems

The linear systems that stem from the discretization methods mentioned above are all sparse and can be rewritten using a straightforward permutation of variables as block banded systems if the boundary conditions are separated:

$$\mathfrak{c}^r(y(0), y(1)) = \begin{bmatrix} r_0(y(0)) \\ r_1(y(1)) \end{bmatrix} .$$

For simplicity, only separated boundary conditions are handled in the current implementation, such that the standard LAPACK band solver can be used. Of course, more sophisticated direct solvers, exploiting the block structure [2]

or even the KKT structure [47], can be expected to decrease the computational cost significantly. Alternatively, iterative solvers may be competitive in the context of inexact Newton methods.

Error Estimation and Adaptive Refinement

In order to achieve the required accuracy demand that is determined by the inexact Newton method via (3.6), a sufficiently fine discretization has to be used. Since the structure of the solution is in general not known a-priori, the computation must be started on an initial *coarse grid* which is subsequently *refined* until a sufficiently good approximation of the solution is available. For the termination of the refinement iteration, an *error estimator* $[\epsilon_{h,q}] \approx \epsilon_h := \|v - v_h\|$ is required.

Moreover, uniform refinement quickly leads to unneccessaryly large discretizations. In particular, in the presence of highly local effects like control switching points, a local refinement of the grid can reduce the approximation error significantly with very few additional discretization variables. Such an *adaptive refinement* uses an *error indicator* to identify intervals that are to be refined.

Utilizing the hierarchical splitting $V_{h,q+1} = V_{h,q} \oplus \bar{V}_{h,q+1}$, where $V_{h,q}$ denotes the finite element space with ansatz functions of polynomial order up to q, a simple error estimator is given by

$$[\epsilon] := \|F_v(v_{h,q+1}; \mu)(I - P_{h,q})v_{h,q+1}\|_{v_{h,q+1}} \,. \tag{4.3}$$

Here, $P_{h,q} : V_{h,q+1} \to V_{h,q}$ denotes the projection to the finite element space of lower polynomial degree by dropping the basis functions of degree $q+1$. An error indicator is obtained by separate evaluation of (4.3) on every mesh subinterval.

For a discussion of more sophisticated weighted error estimators, tailored for optimization problems, we refer to Becker, Kapp, and Rannacher [4].

4.2 Illustrative Examples

To begin with, we apply the proposed method to some small test problems with known solutions.

Example 4.2.1. A vehicle at rest at point A is to be transfered to point B, where it should come to rest, in minimal time. The control is the acceleration which is bounded nonsymmetrically due to different capabilities of engine and brakes. With a very simple model of the underlying mechanics we end up with a linear open end time optimal control problem:

$$\begin{aligned} \min T \quad \text{s.t.} \quad & \dot{y_1} = u \qquad y_1(0) = 0 \qquad y_1(T) = 0 \\ & \dot{y_2} = y_1 \qquad y_2(0) = -1 \qquad y_2(T) = 1 \\ & -1 + a \le u \le 1 + a \,. \end{aligned}$$

Introducing the constant time scaling y_3, this can be rewritten by the chain rule in the form of Section 2.1 as

$$\min \int_0^1 y_3^2 \, dt \quad \text{s.t.} \quad \begin{array}{lll} \dot{y_1} = u y_3 & y_1(0) = 0 & y_1(1) = 0 \\ \dot{y_2} = y_1 y_3 & y_2(0) = -1 & y_2(1) = 1 \\ \dot{y_3} = 0 & & \end{array}$$
$$-1 + a \le u \le 1 + a \,.$$

For $|a| < 1$ the solution is given by the bang-bang control

$$u = \begin{cases} 1 + a, & t < \frac{1-a}{2} \\ -1 + a, & t > \frac{1-a}{2} \end{cases}$$

with the minimal time value of

$$T = \sqrt{\frac{8}{1 - a^2}} \,.$$

The complementarity method suggested here has been applied to this problem with $a = -1/3$, starting at $\mu_0 = 5$ with a value of

$$\begin{array}{lll} u = 0 & \lambda_1 = 0 & \eta_1 = \dfrac{\mu_0}{1 - a} \\ y_1 = \min(t, 1 - t) & \lambda_2 = 0 & \eta_2 = \dfrac{\mu_0}{1 + a} \\ y_2 = 2t - 1 & \lambda_3 = 0 & \\ y_3 = 1 \,. & & \end{array}$$

Figures 4.2 and 4.3 show the approximate central path solutions that are generated in the course of the continuation method. The convergence of the method towards the solution is documented in Figure 4.4, and the mesh generated by adaptive refinement is depicted in Figure 4.5. ◁

Example 4.2.2. This example taken from Bryson and Ho [10] provides a parameter-dependant transition from unconstrained to second order state constrained problems:

$$\min -\frac{1}{2} \int_0^1 u^2 \, dt \quad \text{s.t.} \quad \begin{array}{llll} \dot{y_1} = u & y_1(0) = 1 & y_2(0) = 0 & y_2 \le a \\ \dot{y_2} = y_1 & y_1(1) = -1 & y_2(1) = 0 & \end{array}$$

Depending on the parameter $a > 0$, the state constraint is either inactive for $a > 1/4$, or active in a single touch point for $1/4 \le a \le 1/6$, or on an interval for $a < 1/6$ (cf. Figure 4.6). With $a = 1/9$ we choose the most challenging situation featuring a boundary arc and associated Lagrange multipliers containing Dirac

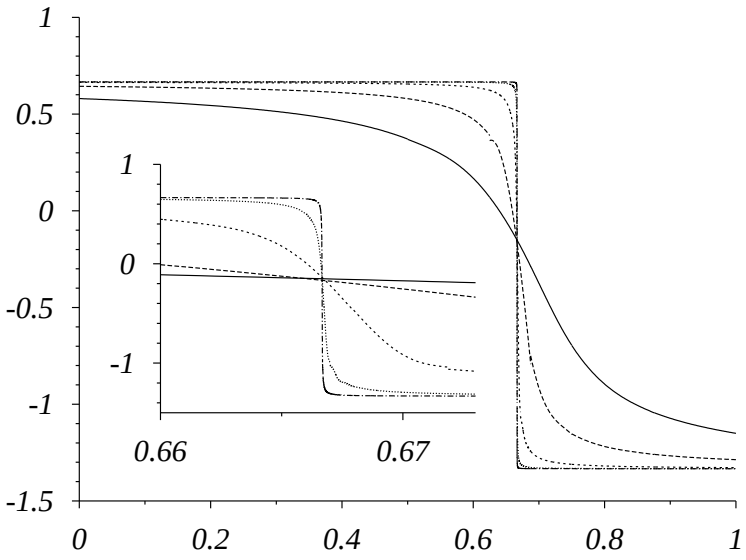

Figure 4.2: Approximate central path solutions of the control u in Example 4.2.1 for $\mu = 5, 0.727, 0.0781, 0.00537, 0.000362$.

functionals at the entry and exit points. For $a < 1/6$ the exact solution is given by

$$y = \begin{cases} a\left(1 - \left(1 - \frac{\frac{1}{2} - \left|t - \frac{1}{2}\right|}{3a}\right)^3\right), & t \leq 3a \text{ or } t \geq 1 - 3a \\ a, & 3a \leq t \leq 1 - 3a \end{cases}$$

with an optimal functional value of $4/9a$. Figures 4.7 and 4.8 show the approximation of the state constraint multiplier. The convergence of the central path solutions is presented in Figure 4.9. Finally, the Newton continuation estimates $[\omega]$ and $[\beta]$ are depicted in Figure 4.10 together with the resulting μ reduction factor. ◁

As can be seen comparing the convergence speed $v(\mu) \to v(0)$, displayed affine invariantly by $\|F(v(\mu); 0)\|_{v(\mu)}$ in Figures 4.4 and 4.9, the state constrained problem is more challenging than the control constrained one. Nevertheless, the convergence in terms of the cost functional value alone is $J(x(\mu)) - J(x^*) \approx \mathcal{O}(\mu)$ in both cases.

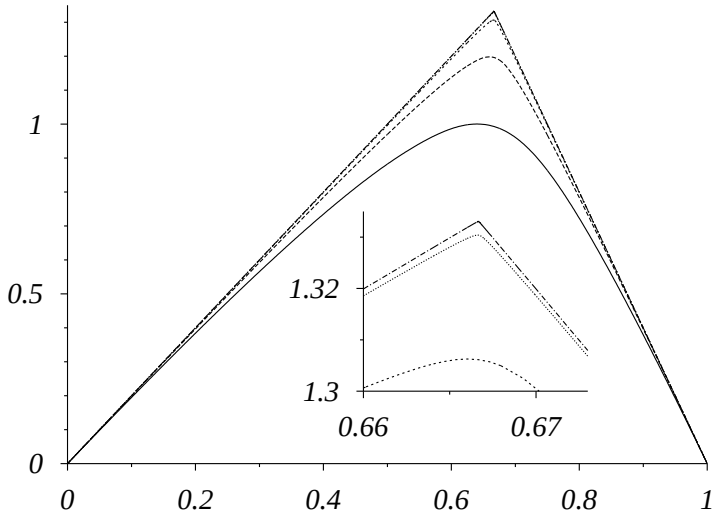

Figure 4.3: Approximate central path solutions of the state derivative y_1 in Example 4.2.1 for $\mu = 5, 0.727, 0.0781, 0.00537, 0.000362$.

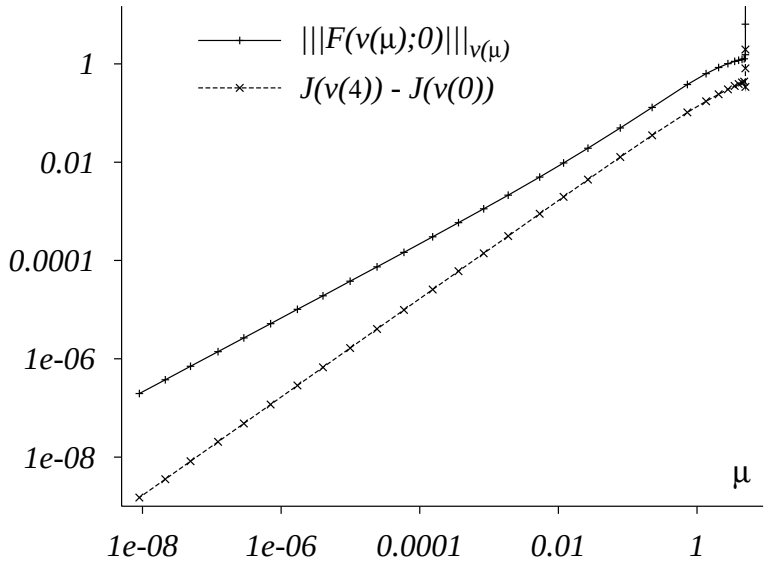

Figure 4.4: Convergence of the central path solutions for the control constrained Example 4.2.1.

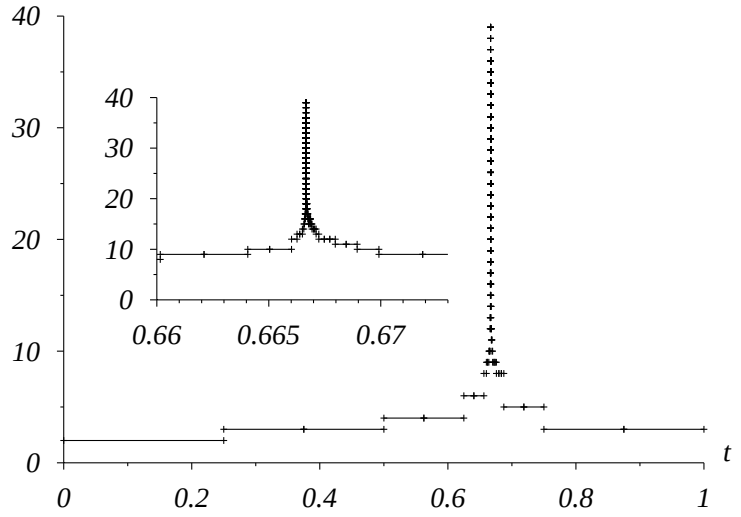

Figure 4.5: Adaptively refined mesh for Example 4.2.1 at $\mu = 9 \cdot 10^{-9}$ generated during the continuation. The value shown is $-\mathrm{ld}h$, where h is the local mesh width. Up to an additive constant this corresponds to the mesh refinement level. Note the massive refinement at the switching point $t = 2/3$, which is difficult to capture by the interval bisection employed.

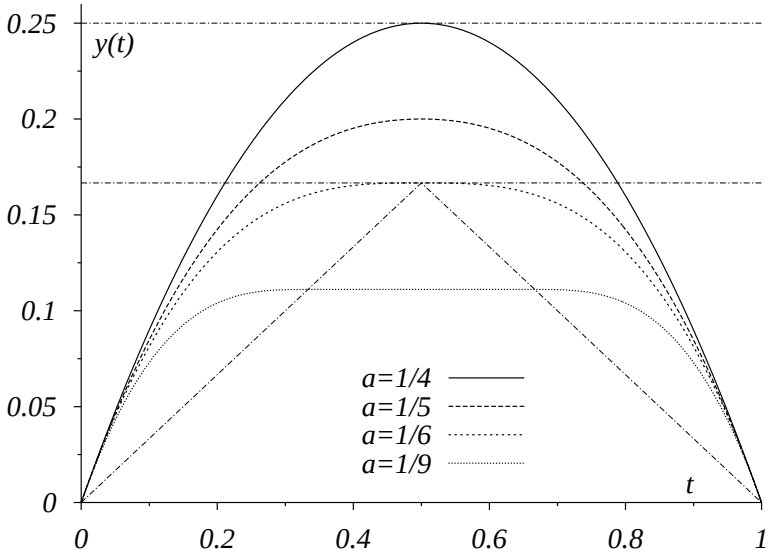

Figure 4.6: Exact solutions of Example 4.2.2 for $a = \frac{1}{4}, \frac{1}{5}, \frac{1}{6}, \frac{1}{8}$.

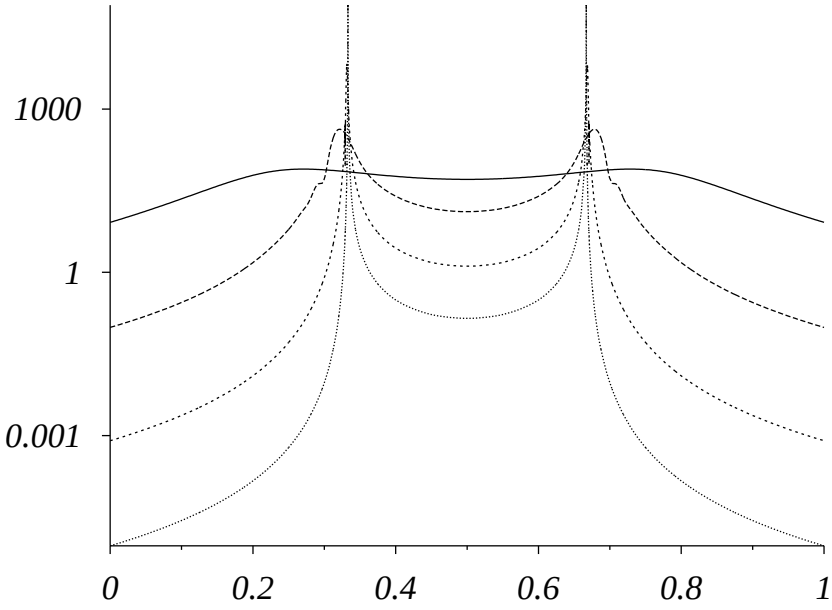

Figure 4.7: State constraint Lagrange multipliers for $\mu = 0.925, 0.0109, 8.95 \cdot 10^{-5}, 1.05 \cdot 10^{-6}$.

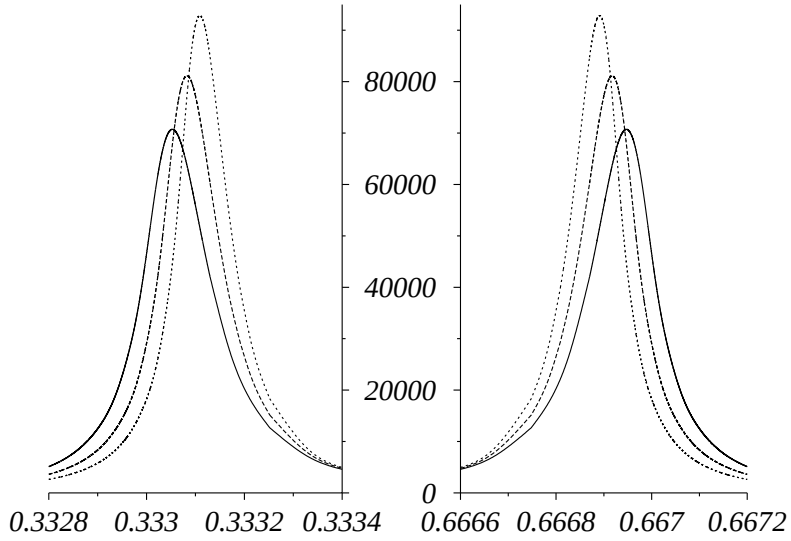

Figure 4.8: Details of the state constraint Lagrange multipliers near the entry and exit points at $t = 1/3$ and $t = 2/3$ for $\mu = 1.15 \cdot 10^{-6}, 9.33 \cdot 10^{-7}, 7.56 \cdot 10^{-7}$.

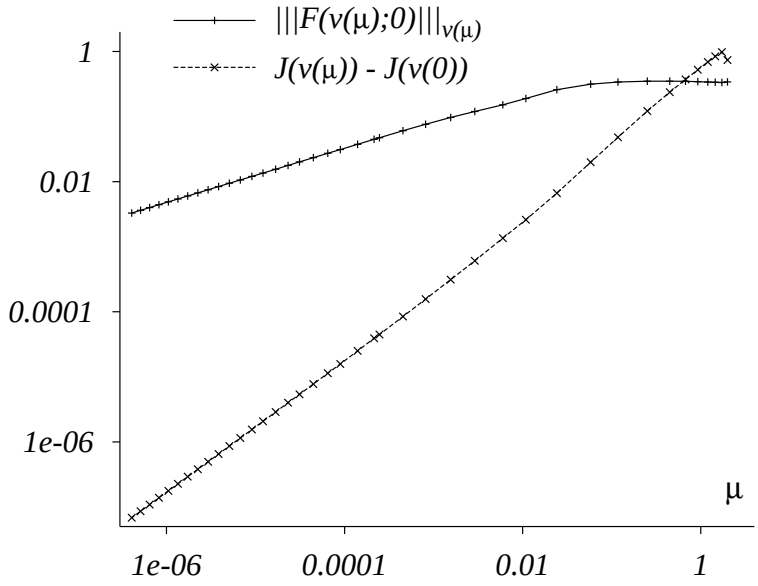

Figure 4.9: Convergence of the central path solutions for the state constrained Example 4.2.2.

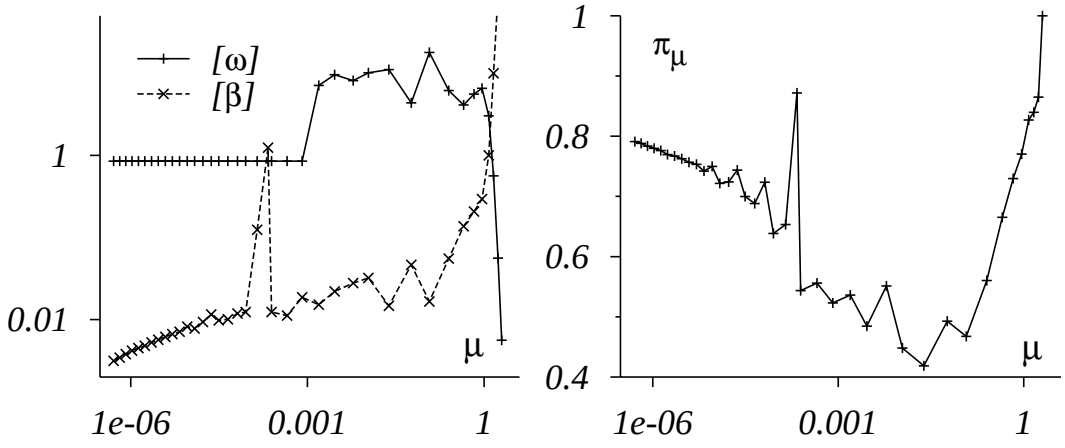

Figure 4.10: Newton continuation estimates $[\omega]$ and $[\beta]$ (left) and μ reduction factors π_μ (right) for Example 4.2.2.

4.3 Abort Landing in the Presence of a Windshear

A more interesting real world example is the abort landing of an airplane crossing a low-altitude windshear. This meteorological phenomenon is usually associated with a column of descending air spreading horizontally near the ground. The subsequential encounter of headwind, downburst, and tailwind during take-off or landing presents one of the most dangerous situations for an aircraft, and is supposed to have caused several accidents in the past (cf. Miele et al. [42]).

In this section we will consider the problem of abort landing that has been analyzed by Miele et al. [42] and Pesch et al. [11, 5]. Abort landing is assumed to be a safer procedure given the initial altitude is sufficiently high. This leads to the Chebyshev-type optimal control problem of maximizing the minimal altitude. Additionally, the problem of maximizing the windshear intensity until the minimal altitude reaches the ground level is of interest.

From a mathematical point of view, the problem is interesting because of its third-order state constraint, its high nonlinearity and the nontrivial switching structure of the optimal solution. The optimal solution features control and state constraint subarcs as well as touch points and singular subarcs, which makes it very difficult to tackle the problem with the maximum principle. In contrast, application of the proposed function space complementarity method turned out to be fairly easy and did not require any in-depth analysis of the model. On the other hand, the extreme accuracy that can be achieved using the maximum principle is not easily reached with the proposed method.

4.3.1 Mathematical Model

To convert the Chebyshev-type optimization problem to the Lagrange formulation that has been assumed throughout the work, we introduce a *lower bound* ζ of the *altitude* h together with the state constraint

$$h \geq \zeta \tag{4.4}$$

and the auxiliary equation

$$\dot{\zeta} = 0\,,$$

such that the cost functional can be written as

$$J = -\int_0^T \zeta \, dt\,.$$

For maximizing the windshear intensity we use $k = \zeta$ together with the altitude constraint $h \geq 0$ instead of (4.4).

$x_1 =$	$5.000 \cdot 10^{2}$	ft	$d =$	$-8.02881 \cdot 10^{-8}$	$s^{-1}ft^{-2}$
$x_2 =$	$4.100 \cdot 10^{3}$	ft	$e =$	$6.28083 \cdot 10^{-11}$	$s^{-1}ft^{-3}$
$x_3 =$	$4.600 \cdot 10^{3}$	ft	$p =$	$5.00000 \cdot 10^{1}$	$s^{-1}ft$
$a =$	$6.000 \cdot 10^{-8}$	$s^{-1}ft^{-2}$	$q =$	$0.0 \cdot 10^{0}$	
$b =$	$-4.000 \cdot 10^{-11}$	$s^{-1}ft^{-3}$	$r =$	$2.50000 \cdot 10^{-2}$	s^{-1}
$c =$	$-10^{-12} \ln(\frac{25}{30.6})$	ft^{-4}	$s =$	$0.0 \cdot 10^{0}$	

Table 4.1: Parameter values for the first wind model.

$x_1 =$	$1.30000 \cdot 10^{3}$	ft	$d =$	$6.45597 \cdot 10^{-8}$	$s^{-1}ft^{-2}$
$x_2 =$	$3.30000 \cdot 10^{3}$	ft	$e =$	$-9.97370 \cdot 10^{-11}$	$s^{-1}ft^{-3}$
$x_3 =$	$4.60000 \cdot 10^{3}$	ft	$p =$	$4.20000 \cdot 10^{1}$	$s^{-1}ft$
$a =$	$-8.55712 \cdot 10^{-8}$	$s^{-1}ft^{-2}$	$q =$	$-3.87834 \cdot 10^{-14}$	
$b =$	$-1.16943 \cdot 10^{-10}$	$s^{-1}ft^{-3}$	$r =$	$4.00000 \cdot 10^{-2}$	s^{-1}
$c =$	$9.50000 \cdot 10^{-13}$	ft^{-4}	$s =$	$3.32076 \cdot 10^{-14}$	

Table 4.2: Parameter values for the second wind model.

Horizontal and *vertical wind velocity* is given by

$$W^x = kA(x)$$
$$W^h = k\frac{h}{h_\star}B(x)$$

with

$$A(x) = \begin{cases} -p + ax^3 + bx^4 + qx^5, & 0 \le x \le x_1 \\ r(x - \frac{x_3}{2}), & x_1 \le x \le x_2 \\ p - a(x_3 - x)^3 - b(x_3 - x)^4 - q(x_3 - x)^5, & x_2 \le x \le x_3 \\ p, & x_3 \le x \end{cases}$$

$$B(x) = \begin{cases} dx^3 + ex^4 + sx^5, & 0 \le x \le x_1 \\ -51 \exp(-c(x - \frac{x_3}{2})^4), & x_1 \le x \le x_2 \\ d(x_3 - x)^3 + e(x_3 - x)^4 + s(x_3 - x)^5, & x_2 \le x \le x_3 \\ 0, & x_3 \le x \end{cases}.$$

Here, the parameter k characterizes the windshear intensity. The parameter sets for the two different wind models from [5] are given in Tables 4.1 and 4.2.

Note that both wind models have discontinuous higher derivatives at the junction points x_1, x_2, and x_3. The first wind model is C^1 whereas the second is C^2.

$A_0 =$	$4.4560{\cdot}10^{4}$	lb	$B_0 = 1.5520{\cdot}10^{-1}$	
$A_1 =$	$-2.3980{\cdot}10^{1}$	lb s ft^{-1}	$B_1 = 1.2369{\cdot}10^{-1}$	rad^{-1}
$A_2 =$	$1.4420{\cdot}10^{-2}$	lb s^{2}ft^{-2}	$B_2 = 2.4203{\cdot}10$	rad^{-2}
$C_0 =$	$7.2150{\cdot}10^{-1}$		$\rho = 2.2030{\cdot}10^{-3}$	lb s^{2}ft^{-4}
$C_1 =$	$6.0877{\cdot}10^{0}$	rad^{-1}	$S = 1.5600{\cdot}10^{3}$	ft^2
$C_2 =$	$-9.0277{\cdot}10^{0}$	rad^{-2} for $p_L = 2$	$\alpha_\star = 2.0944{\cdot}10^{-1}$	rad
	$-1.0000{\cdot}10^{2}$	rad^{-2} for $p_L = 3$	$\delta = 3.4906{\cdot}10^{-2}$	rad
$mg =$	$1.5000{\cdot}10^{5}$	lb	$g = 3.2172{\cdot}10^{1}$	s^{-2}ft

Table 4.3: Parameter values for the aerodynamic forces.

$\beta_0 = 3.825{\cdot}10^{0}$	
$\dot\beta_0 = 2.000{\cdot}10^{-1}$	s^{-1}

Table 4.4: Model parameter data for the power setting.

Under the assumption of the airplane to be a particle of constant mass moving in a vertical plane and the wind field to be steady, the following equations of motion can be derived:

$$\begin{aligned}
\dot x &= V\cos\gamma + W^x \\
\dot h &= V\sin\gamma + W^h \\
\dot V &= \frac{T}{m}\cos(\alpha+\delta) - \frac{D}{m} - g\sin\gamma - (\dot W^x\cos\gamma + \dot W^h\sin\gamma) \\
V\dot\gamma &= \frac{T}{m}\sin(\alpha+\delta) + \frac{L}{m} - g\cos\gamma + (\dot W^x\sin\gamma - \dot W^h\cos\gamma) \\
\dot\alpha &= u\,.
\end{aligned}$$

Here, x denotes the *horizontal position*, h the *altitude*, V the *relative velocity*, γ the *relative path inclination*, and α the *relative angle of attack*. The derivative of the angle of attack u is chosen as control variable. Note that due to the occurrence of the derivatives $\dot W^x$ and $\dot W^h$ in the equations of motion, the problem is C^2 as assumed by the theory only if the wind model functions A and B are C^3.

Approximations for the *aerodynamic forces* thrust T, drag D, and lift L acting on the aircraft are given by

$$T = \beta(A_0 + A_1V + A_2V^2) \tag{4.5}$$

$$D = \frac{1}{2}(B_0 + B_1\alpha + B_2\alpha^2)\rho SV^2 \tag{4.6}$$

$$L = \frac{1}{2}(C_0 + C_1\alpha + C_2\max(0,\alpha-\alpha_\star)^{p_L})\rho SV^2 \tag{4.7}$$

$u_{\max}$=5.236·10^{-2}	rad s^{-1}
$\alpha_{\max}$=3.002·10^{-1}	rad

Table 4.5: Model parameter data for the inequality constraints.

initial conditions		terminal conditions	
x_0=0.0 ·10	ft	t_f =4.000·10^1	s
γ_0=3.925·10^{-2}	rad	γ_f=1.297·10^{-1}	rad
α_0=1.283·10^{-1}	rad		
h_0=6.000·10^2	ft		
V_0=2.397·10^2	ft s^{-1}		

Table 4.6: Model parameter data for boundary conditions.

with the *power setting*

$$\beta = \min(1, \beta_0 + \dot{\beta}_0 t)$$

resulting from the additional hypothesis that, upon sensing the aircraft to be in a windshear, the pilot increases the power setting at a constant time rate until the maximum power setting is reached. The lift approximation from [11] with $p_L = 2$ has a discontinuous second derivative. Changing p_L to 3 and adjusting C_2 accordingly, a twice continuously differentiable lift equation can be used instead. The model parameter data given in Table 4.3 refer to a Boeing B727 aircraft powered by three JT8D-17 turbofan engines.

Simple *bounds* are imposed on the angle of attack and its derivative:

$$|u| \leq u_{\max}$$
$$\alpha \leq \alpha_{\max}$$

Boundary conditions are given for the initial quasi-steady flight prior to the windshear onset and for terminal steepest climb in quasi-steady flight:

$$x(0) = x_0 \qquad V(0) = V_0$$
$$h(0) = h_0 \qquad \gamma(0) = \gamma_0$$
$$\gamma(t_f) = \gamma_f \,.$$

4.3.2 Numerical Results

Strictly speaking, neither the lift equation (4.7) nor the wind models are sufficiently smooth and therefore leave our above theoretical frame. Nevertheless,

as will be shown, the highly accurate results obtained in [11, 5] by multiple shooting are surprisingly well reproduced by the complementarity approach suggested here. Figures 4.11 to 4.14 show altitude, path inclination, angle of attack, and angle of attack rate in direct comparison of the two methods.

Significant differences in the computed solutions occur for $t > t_* = 25.997s$. The reason for the deviation is that there is no unique optimal trajectory. After the last point of minimal altitude has been reached, the value of the control u influences the trajectory, but no longer its minimal altitude. Therefore, a whole continuum of optimal trajectories exist, all of them differing only after the last touch point of $h = \zeta$. Similar to the situation in Example 2.2.6, this is already indicated by the vanishing Lagrange multipliers of the equality constraints, which are equal to zero for $t > t_*$ as depicted in Figure 4.15. The indirect multiple shooting method and the complementarity method as suggested here just happen to pick different optimal trajectories from a continuum.

In Figure 4.16 the mesh refinement structure is shown. To achieve the high precision, a massive refinement at the relevant points is necessary. Obviously, the highly dynamic structure of the solution is captured reasonably well by the adaptive refinement procedure. Newton continuation estimates and μ reduction factors are shown in Figure 4.17, the convergence of the central path approximations in Figure 4.18. In contrast to the linear examples in Section 4.2, the continuation step size is limited by both the estimated curvature and the feasibility requirement.

For the second wind model, the solution has been obtained in [5] using a homotopy in the wind model parameters x_1, c, r, and p. During the homotopy computation, the intermediate solutions have to be checked carefully for changes of the switching structure. In case of changing switching structure, the interior boundary conditions and the right hand sides of the adjoint differential equations must be appropriately adjusted. Table 4.7 gives an overview over the different switching structures that occur in the course of the homotopy and is provided here to give an impression of the amount of detailed analysis of the problem that is required by indirect methods.

Again, the complementarity method is able to reach the solution depicted in Figures 4.19 and 4.20 without any preparatory analytical work.

param[(a)]	switching structure												
$x_1 = 500$	$-$		s	h	s	$\langle + \rangle$	s	$\langle \alpha \rangle$		$-$			
$= 1300$	unchanged												
$c \approx 0.2021$	see $x_1 = 1300$												
$= 0.4525$	$-$		$\langle s \rangle$	h	s	$\langle + \rangle$		$\langle \alpha \rangle$		$-$			
$= 0.7$	$+$		$\langle s \rangle$	h	s	$\langle + \rangle$		$\langle \alpha \rangle$		$-$			
$= 0.8$	$+$			$\langle\langle s \rangle\rangle$		$\langle + \rangle$		$\langle \alpha \rangle$		$-$			
$= 0.9$	$+$		s	h	$\langle s \rangle$	$\langle + \rangle$		$\langle \alpha \rangle$		$-$			
$= 0.95$	$+$		s	h	s	$\langle + \rangle$		$\langle \alpha \rangle$		$-$			
$r = 0.025$	see $c = 0.95$												
$= 0.026$	$+$			$\langle s \rangle$		$\langle + \rangle$		$\langle \alpha \rangle$		$-$			
$= 0.029$	$+$			$\langle s \rangle$		$\langle + \rangle$	s	$\langle \alpha \rangle$		$-$			
$= 0.033$	$-$			$\langle s \rangle$		$\langle + \rangle$	s	$\langle \alpha \rangle$		$-$			
$= 0.039$	$-$			$\langle s \rangle$		$\langle + \rangle$	s	α	$\langle\rangle$	$-$	$+$	α	
$= 0.04$	see $r = 0.039$												
$p = 0.05$	see $r = 0.039$												
$= 0.047$	$+$			$\langle s \rangle$		$\langle + \rangle$	s	α	$\langle\rangle$	$-$	$+$	α	
$= 0.044$	$+$		s	h	s	$\langle + \rangle$	s	α	$\langle\rangle$	$-$	$+$	α	
$= 0.042$	$+$	$-$	s	h	s	$\langle + \rangle$	s	α	$\langle\rangle$	$-$	$+$	α	

notation for switching structure	
$+$	$u = u_{\max}$
$-$	$u = u_{\min}$
s	singular control subarc
h	altitude constrained subarc
α	angle of attack constrained subarc
$\langle\diamondsuit\rangle$	one touch point in the interior of subarc $\diamondsuit$
$\langle\langle\diamondsuit\rangle\rangle$	two touch points in the interior of subarc $\diamondsuit$
$\langle\rangle$	touch point right at the junction of two subarcs

Table 4.7: Survey of the switching structures that occur during the homotopy from the first to the second wind model. This is a part of Table 5 from [5].
[(a)] Homotopy parameters near which or starting at which a change of the switching structure occurs.

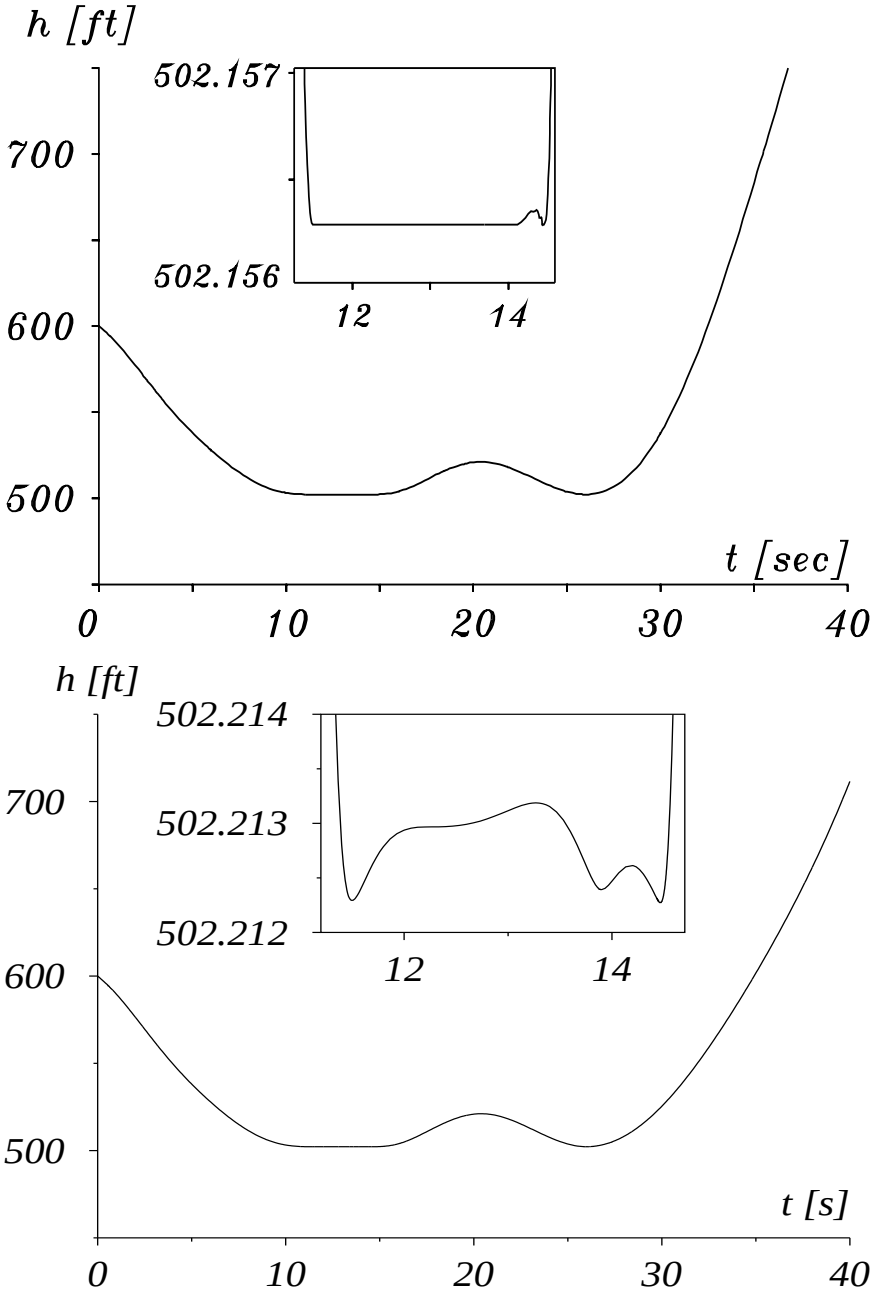

Figure 4.11: Altitude h versus time for the first wind model ($k = 1$). Top: result from [5]. Bottom: complementarity solution at $\mu = 2.1 \cdot 10^{-4}$.

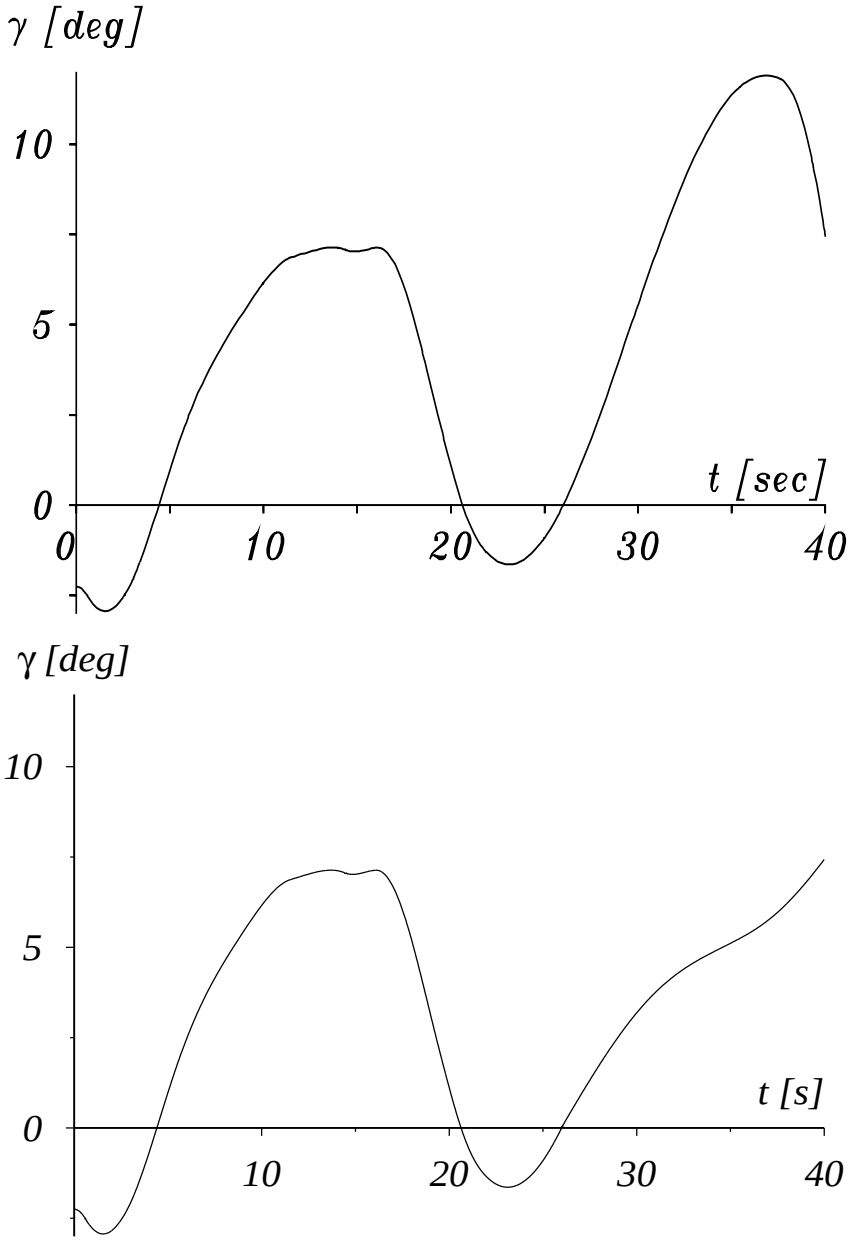

Figure 4.12: Path inclination γ versus time for the first wind model ($k = 1$). Top: result from [5]. Bottom: complementarity solution at $\mu = 2.1 \cdot 10^{-4}$.

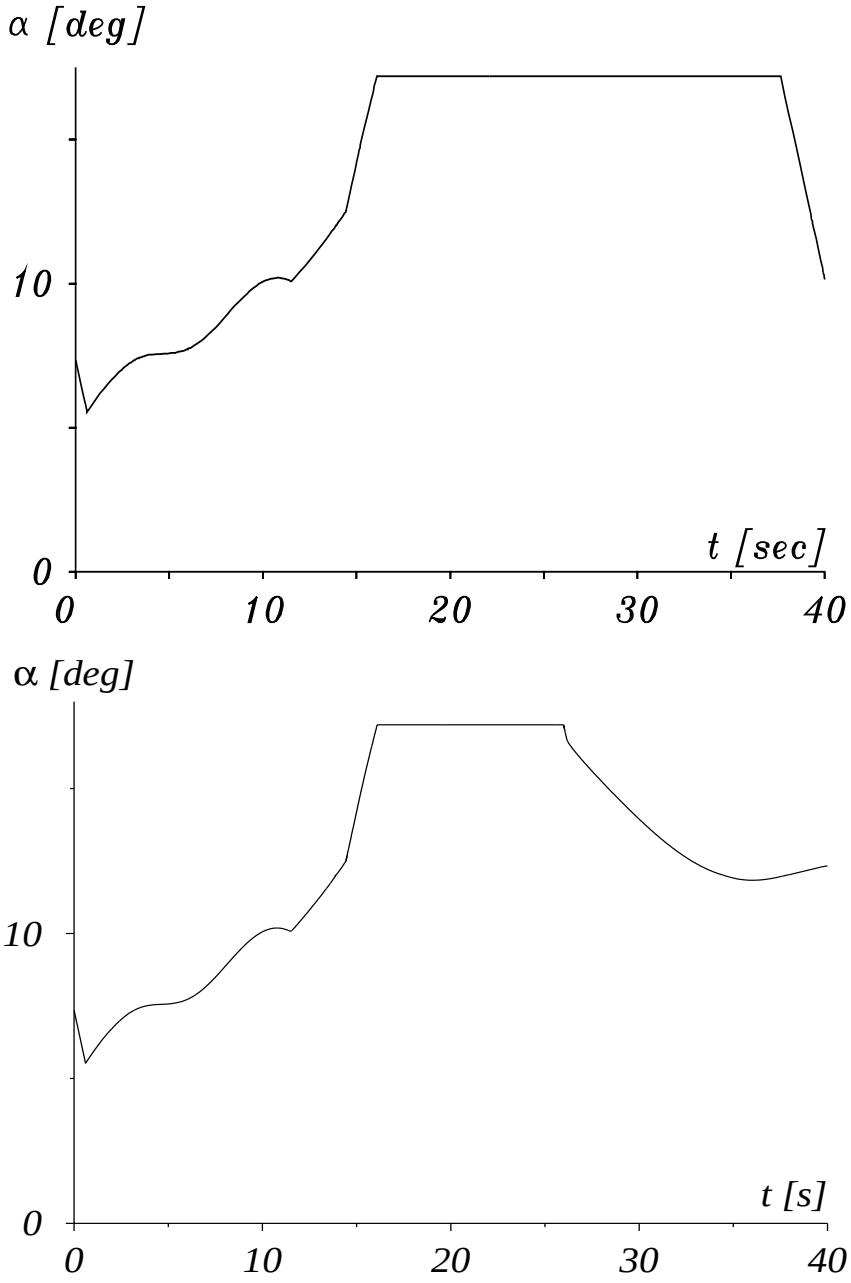

Figure 4.13: Angle of attack α versus time for the first wind model ($k = 1$). Top: result from [5]. Bottom: complementarity solution at $\mu = 2.1 \cdot 10^{-4}$.

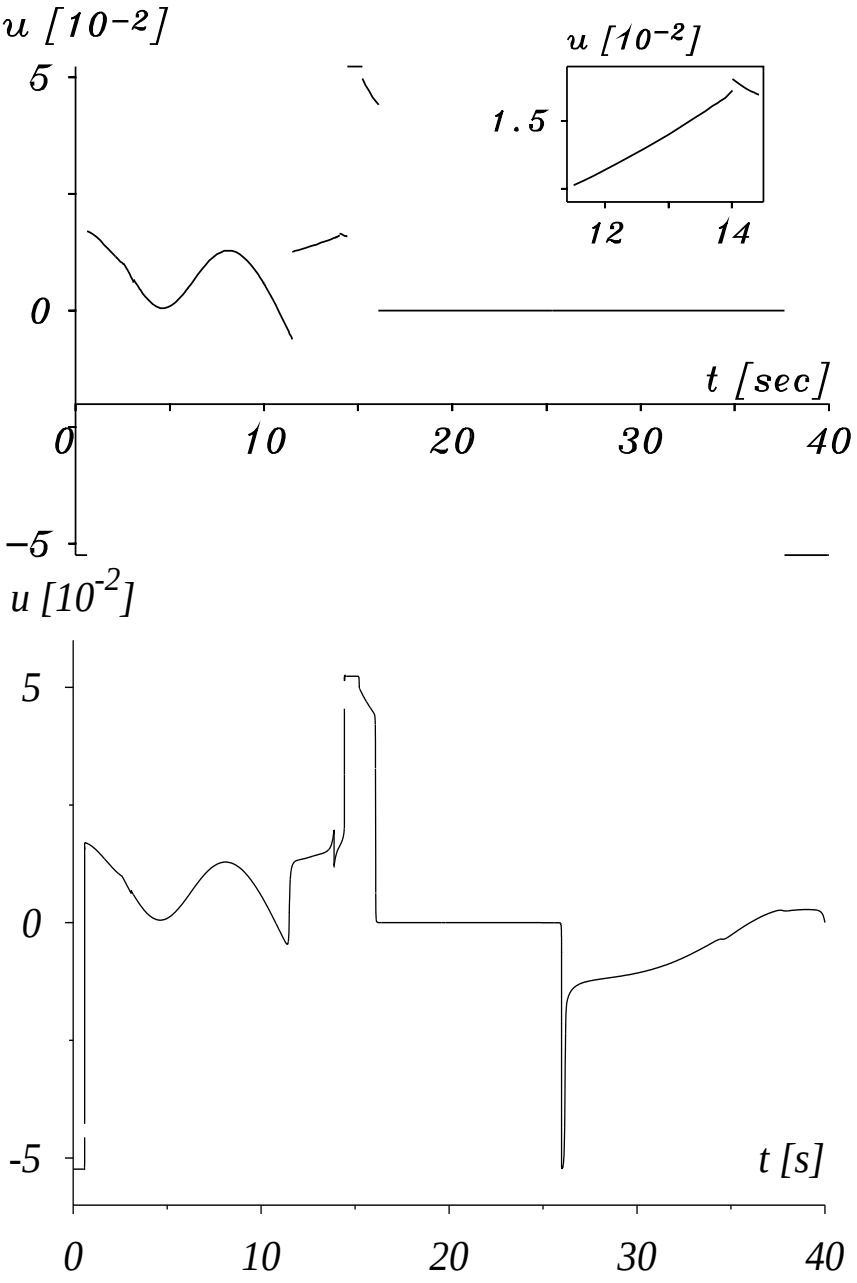

Figure 4.14: Angle of attack rate u (control) versus time for the first wind model ($k = 1$). Top: result from [5]. Bottom: complementarity solution at $\mu = 2.1 \cdot 10^{-4}$.

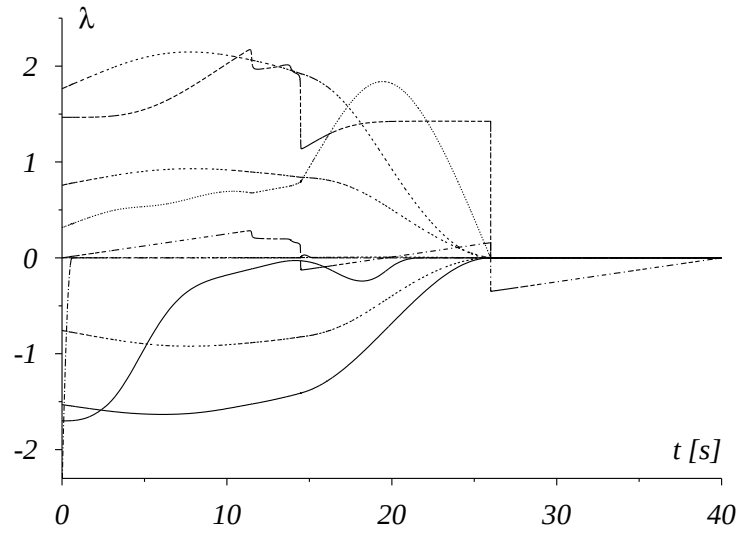

Figure 4.15: Lagrange multipliers λ_i of the equality constraints. The multipliers are scaled to the same order of magnitude. Note that all multipliers except the one corresponding to the Chebyshev reformulation $\dot{\zeta} = 0$ vanish for $t > t_* = 25.997s$.

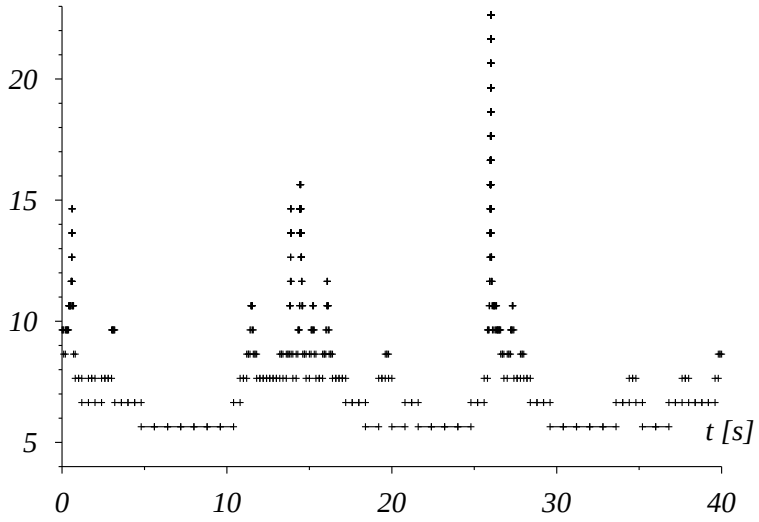

Figure 4.16: Mesh refinement structure. The value shown is $-\mathrm{ld}h$, where h is the local mesh width. Up to an additive constant this corresponds to the mesh refinement level. Note the massive refinement at the switching and contact points.

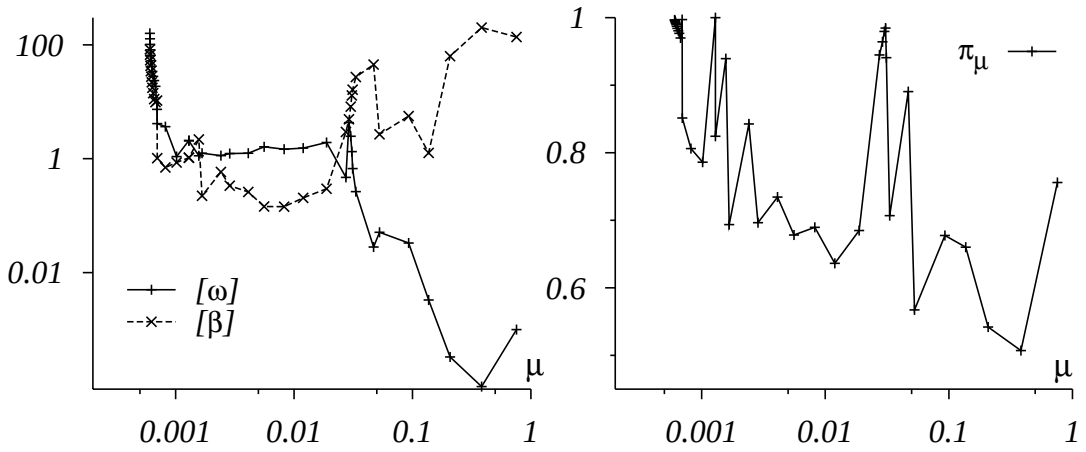

Figure 4.17: Newton continuation estimates $[\omega]$ and $[\beta]$ (left) and the μ reduction factors π_μ (right) for the first wind model.

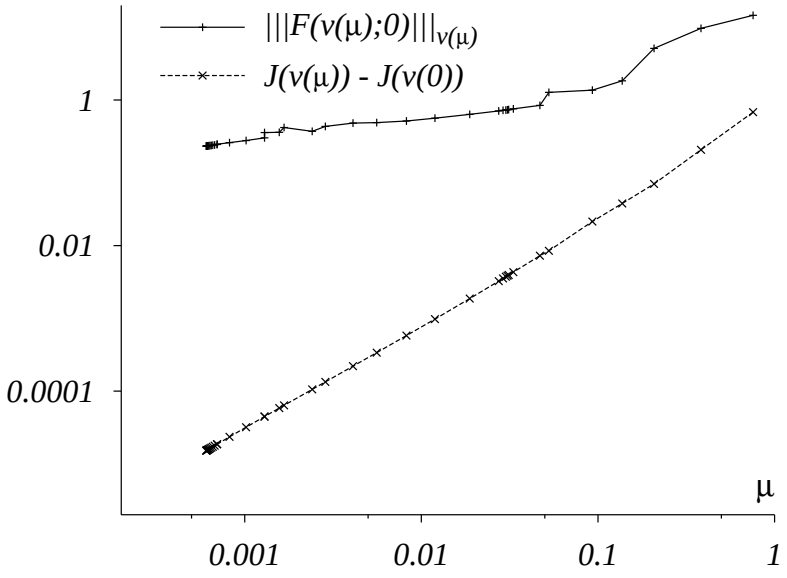

Figure 4.18: Convergence of the central path solutions for the first wind model.

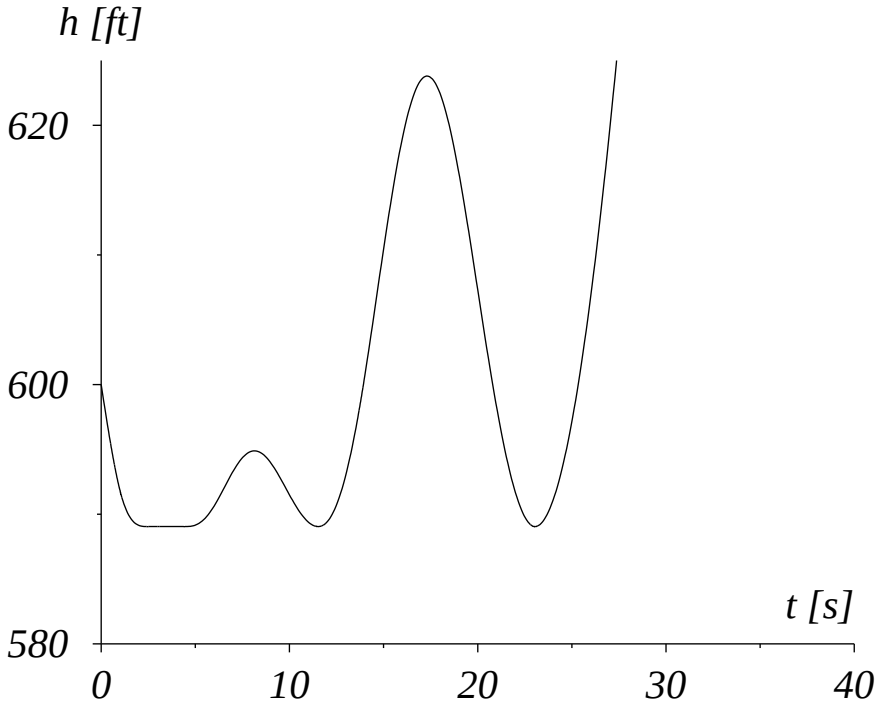

Figure 4.19: Altitude h versus time for the second wind model. Complementarity solution at $\mu = 4.3 \cdot 10^{-4}$.

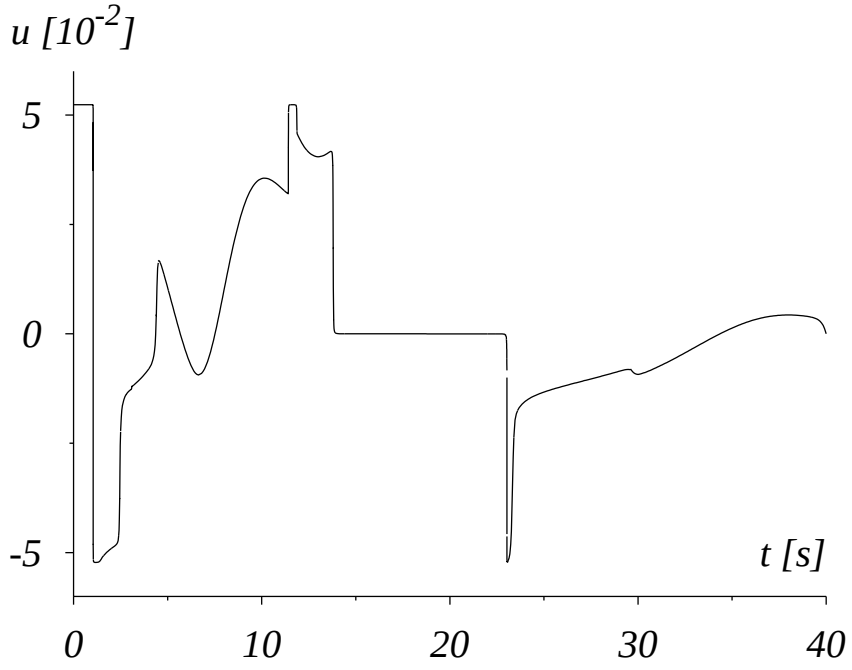

Figure 4.20: Control u versus time for the second wind model. Complementarity solution at $\mu = 4.3 \cdot 10^{-4}$.